ISSN 1392-1320 MATERIALS SCIENCE (MEDŽIAGOTYRA). Vol. XX, No. X. 2026

Effect of Laser Shock Peening on Dissimilar AA6061-T6/Pure Copper Friction Stir Spot Welded Joints

Sarah Khazaal Jabbar MADHI [1], İsmail Hakkı KARA [1], Rasha M. HUSSEIN [2] *

[1] *Department of Metallurgy and Materials, Faculty of Engineering, Karabük University, Karabük 78050, Turkey*
[2] *Department of Mechanical Engineering, University of Technology, Baghdad 19006, Iraq*

http://doi.org/10.5755/j02.ms.45052

Received 19 May 2026; accepted 1July 2026

Friction Stir Spot Welding (FSSW) is a solid-state route for joining dissimilar aluminum-copper assemblies, but welding-induced softening and the brittle Al-Cu intermetallic layer limit joint reliability. This work investigates the integrated use of FSSW and Laser Shock Peening (LSP) as a post-weld surface treatment for 3 mm thick AA6061-T6/pure copper lap joints. A Taguchi L9 array with ANOVA was used to optimize rotational speed, dwell time, and tool geometry, identifying tool shape as the dominant factor; the optimum joint was then treated by LSP with a Q-switched Nd:YAG laser and compared with the as-welded baseline. The joint exhibited an asymmetric response: the aluminum side recovered its HAZ softening and exceeded its base-metal hardness, while the copper side softened slightly through laser-induced thermal recovery, yet the joint showed a net strengthening. XRD and FTIR supported grain refinement and the absence of thermal-oxidation damage. The integrated FSSW + LSP route is thus proposed as a viable post-weld strengthening strategy for thick dissimilar Al/Cu joints.

Keywords: AA6061-T6, dissimilar joining, friction stir spot welding, laser shock peening, pure copper, microhardness, Taguchi optimization.

1. INTRODUCTION

Metals and engineering materials serve as the foundational pillars of modern industry, where their specific mechanical and physical attributes are essential for performance in sectors from aerospace to electrical engineering [1]. The combination of copper and aluminum is a prime example of this approach: aluminum offers low density and high corrosion resistance, while copper provides exceptional electrical and thermal conductivity. Their integration is therefore highly desirable for electrical bus-bars, battery interconnects, automotive heat-exchangers, and aerospace cable-shielding components [2, 3]. However, the joining of dissimilar Al-Cu pairs by conventional fusion welding is severely limited by the formation of brittle intermetallic compounds (IMCs) such as $CuAl_2$ and Cu_9Al_4, which act as crack-initiation sites and significantly compromise the joint strength [4, 5]. Beyond their mechanical penalty, these interfacial IMCs are also electrically detrimental: the room-temperature resistivity of $CuAl_2$ and Cu_9Al_4 ($\approx 6-13$ μΩ cm) is roughly four to eight times that of pure copper (≈ 1.7 μΩ cm), so a continuous IMC band markedly raises the contact resistance of the joint and degrades its current-carrying capability, a critical limitation for the electrical Al–Cu interconnects targeted here.

To address these limitations, solid-state welding processes operating below the melting point of the materials have been developed to suppress IMC formation and avoid the metallurgical defects associated with fusion-based techniques [6 – 8]. Friction Stir Spot Welding (FSSW) is a revolutionary solid-state joining technology, invented and developed by The Welding Institute (TWI) in 1991. The process utilizes a non-consumable rotating tool, comprising a shoulder and a pin, that plunges into the overlapping sheets and generates frictional heat without reaching the melting point of the parent materials [9, 10]. The plasticized material is then mechanically stirred and forged under the shoulder pressure, producing a metallurgical bond at the lap interface. Owing to its low heat input, low distortion, short cycle time, and the absence of shielding gas, FSSW has become an attractive alternative to resistance spot welding and riveting in the automotive, aerospace, and electrical industries [11, 12].

Despite the advantages of FSSW, dissimilar Al-Cu joining remains challenging. The welding thermal cycle introduces tensile residual stresses on the precipitation-hardenable aluminum side and produces a softened Heat-Affected Zone (HAZ) due to the dissolution and over-ageing of the β-Mg_2Si strengthening precipitates of the AA6061-T6 alloy [13, 14]. The persistent Al-Cu IMC layer and the welding-induced softening remain the principal limitations to joint reliability and fatigue performance [15, 16]. Several recent works have systematically investigated dissimilar FSSW of Al-Cu pairs. Habba and Ahmed [17] reviewed enhancement strategies and identified tool geometry and stacking sequence as the dominant variables. Fuse et al. [18] compared conventional and bobbin-tool FSW of Al/Cu and reported that the Cu-on-top configuration yielded the highest tensile-shear load. Mao et al. [19] characterized the IMC band of micro-FSW Al/Cu ultra-thin sheets and confirmed the role of $CuAl_2$ and Cu_9Al_4 in joint failure. Carlone et al. [20] documented the microstructural aspects of Al-Cu FSW and highlighted the

* Corresponding author: İ. H. Kara
E-mail: *ihakkikara@karabuk.edu.tr*

role of moderate heat input in disrupting continuous IMC bands. Process-parameter optimization is essential to maximize joint strength while limiting IMC growth. The Taguchi method, based on orthogonal arrays and signal-to-noise (S/N) ratio analysis, has been widely applied to FSW and FSSW process design because it minimizes the number of experimental runs required to identify optimum factor levels [21 – 23]. Manickam et al. [22] applied a Taguchi L9 array to dissimilar AA6061/AZ31B FSSW joints and identified the rotational speed as the dominant factor. Ahmed et al. [24] used a Taguchi design to optimize bobbin-tool FSW of aluminum and reported that the dwell-time exposure was a critical thermal-input variable. Concerning to tool geometry, Arumugam et al. [25] reviewed FSSW tool designs and showed that polygonal pin profiles (square, hexagonal) generate a pulsed plastic-strain field that enhances material mixing relative to cylindrical pins, while Kumar and Chander [26] confirmed that tool-pin geometry is a dominant variable for the mechanical performance of dissimilar AA5083/AA6061 joints.

To mitigate welding-induced HAZ softening and convert the residual-stress field into a compressive one, several mechanical surface treatments have been applied to FSW joints, including pull-punching, shot peening, and Laser Shock Peening (LSP) [27 – 29]. Among these, LSP offers a unique combination of high strain-rate ($\approx 10^6$ s^{-1}), localized energy deposition, and a deep compressive layer, with no thermal damage when applied through a transparent dielectric overlay [30 – 32]. Hatamleh et al. [33 – 35] demonstrated that LSP applied to FSW AA7075-T7351 reduced the fatigue crack growth rate by approximately one order of magnitude, while Balos et al. [36] showed a significant increase in microhardness in the HAZ of bobbin-tool FSW AW6060 after LSP. Su et al. [37] reported a similar fatigue-life enhancement for AA6061 welded joints treated by LSP. Despite this growing body of work, no systematic study has been reported on the integrated FSSW + LSP processing of thick (≥ 3 mm) dissimilar AA6061-T6/pure copper lap joints.

The present work addresses this gap. Three FSSW process parameters rotational speed, dwell time, and tool pin geometry are optimized using a Taguchi L9 orthogonal array with maximum tensile-shear load as the response variable; analysis of variance is additionally performed to quantify the contribution of each factor. The optimum joint is then subjected to LSP using a Q-switched Nd: YAG laser, and the as-welded and LSP-treated joints are compared in terms of microhardness distribution, microstructural evolution, phase content (XRD), and surface chemistry (FTIR). The novelty of this work is twofold: it documents the first systematic application of LSP as a post-weld treatment to thick dissimilar AA6061-T6/pure Cu FSSW lap joints, and it identifies and rationalizes a previously unreported asymmetric LSP response between the two base materials, which has direct implications for the engineering design of integrated FSSW + LSP routes.

2. EXPERIMENTAL DETAILS

2.1. Materials and chemical composition

Two dissimilar base metals were selected to fabricate the dissimilar joints: aluminum alloy 6061-T6 and commercially pure copper, both supplied as 3 mm thick sheets. The chemical compositions were verified by atomic emission spectroscopy using an ARL3460 Spectro Maxx instrument, and the results are reported in Table 1 and Table 2 together with the corresponding standard specifications. The measured compositions fall within the ASTM ranges for both alloys, confirming the certified grade of the as-received sheets. The AA6061-T6 was used in the as-supplied artificial-ageing condition, while the Cu was tested in the soft-annealed state. The complete experimental flowchart of the present work is shown in Fig. 1.

2.2. Friction stir spot welding process

Lap-shear specimens of dimensions 100 × 30 × 3 mm were prepared from each base metal and were rigidly secured using a mild-steel fixture. The welding tool was machined from H13 hot-work tool steel [38] and consisted of a flat shoulder of 12 mm in diameter and a threaded pin of 5 mm in diameter and 2.8 mm in length. Three pin geometries cylindrical, square, and hexagonal were investigated to assess the influence of the pin profile on the material flow and IMC distribution [25, 26]. Welding was performed on a computer-controlled vertical milling machine at room temperature.

Preliminary screening tests were carried out at 1450 rpm and 120 s with a cylindrical pin to identify the optimal stacking sequence. Two configurations were tested: AA6061-T6 on top/pure Cu at the bottom, and the inverse arrangement. Tensile-shear testing showed that the Al-on-top configuration consistently failed at 1.46 kN, while the Cu-on-top configuration produced sound joints with a maximum load of 1.89 kN. This asymmetry is attributed to the relatively lower hardness and higher ductility of copper, which permits a smoother material flow around the rotating tool pin and a more effective mechanical interlocking around the lap interface. Consequently, the Cu-on-top arrangement was adopted for the main optimization study.

Table 1. Standard and measured chemical composition (wt.%) of AA6061-T6

Material	Si	Fe	Cu	Mn	Mg	Cr	Zn	Ti	Al
Standard	0.4 – 0.8	< 0.7	0.15 – 0.4	< 0.15	0.8 – 1.2	< 0.25	< 0.15	0.04 – 0.35	Bal.
Measured	0.616	0.328	0.235	0.054	0.998	0.217	0.005	0.032	Bal.

Table 2. Standard and measured chemical composition (wt.%) of pure copper

Material	Bi	Fe	Pb	O	Cu
Standard	< 0.001	< 0.005	< 0.005	< 0.040	> 99.90
Measured	< 0.001	0.003	0.002	0.026	99.95

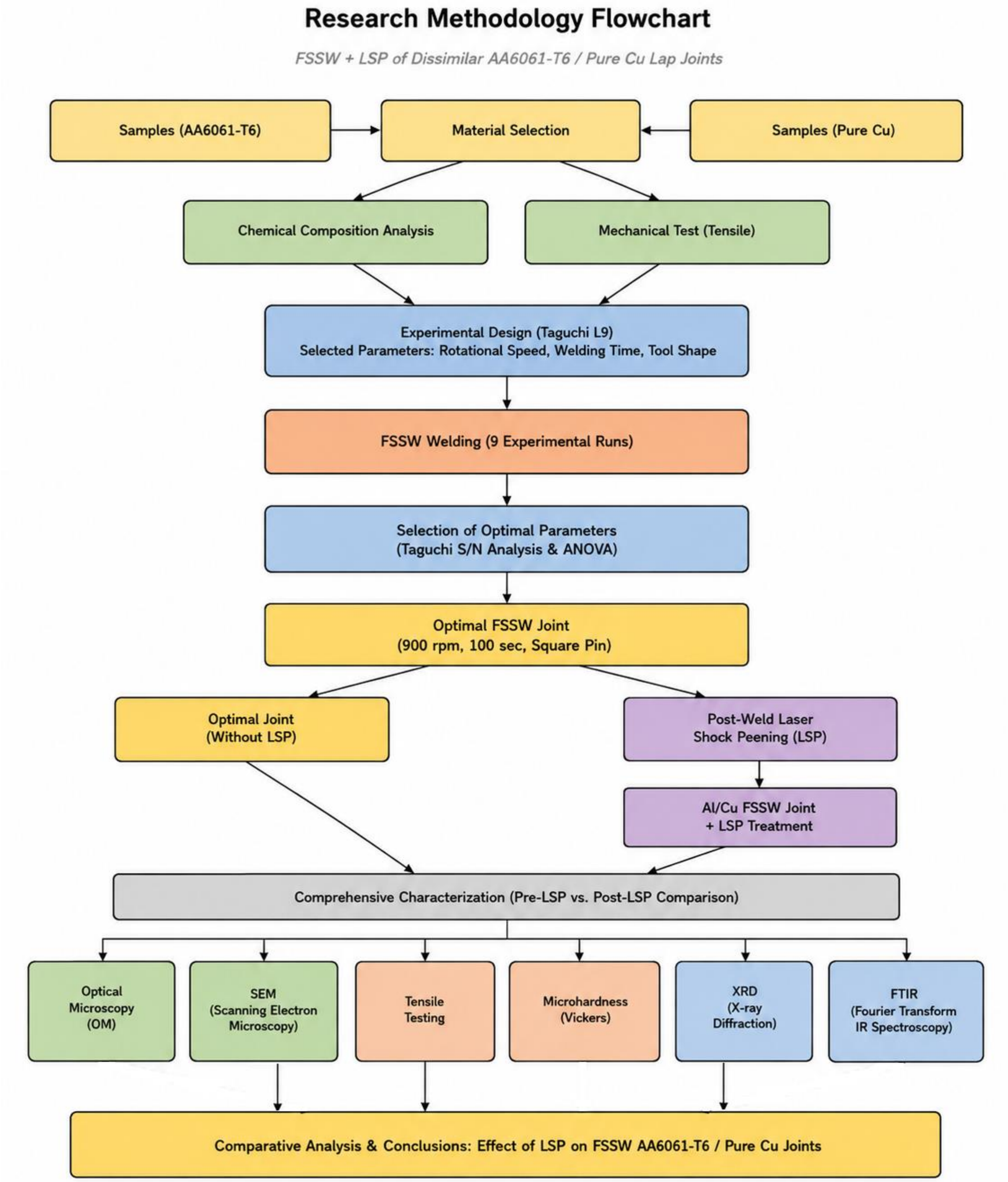

Fig. 1. Schematic flowchart of the experimental methodology adopted in the present work, integrating Friction Stir Spot Welding (FSSW) of dissimilar AA6061-T6/pure Cu lap joints with post-weld Laser Shock Peening (LSP) treatment, followed by mechanical, microstructural, and surface-chemistry characterization

The macroscopic appearance of representative welded lap-shear specimens produced at the optimum parameters is shown in Fig. 2.

A Taguchi L9 orthogonal array was used to optimize three process parameters with three levels each: rotational speed (900, 1450, 1800 rpm), dwell time (100, 120, 140 s), and pin geometry (cylindrical, square, hexagonal). The relatively extended dwell-time window adopted in the present work was deliberately chosen for two interrelated reasons. First, the dissimilar AA6061-T6/pure Cu pair has a substantial mismatch in thermal conductivity (Cu ≈ 401 W m^{-1} K^{-1} versus Al ≈ 167 W m^{-1} K^{-1}) and in melting point, which makes the pure-copper sheet a strong heat sink. Second, the 3 mm sheet thickness requires longer thermal exposure to achieve effective plasticization of the bottom Al sheet through the colder Cu top sheet. The factor-level matrix is summarized in Table 3, and the L9 run Table is given in Table 4.

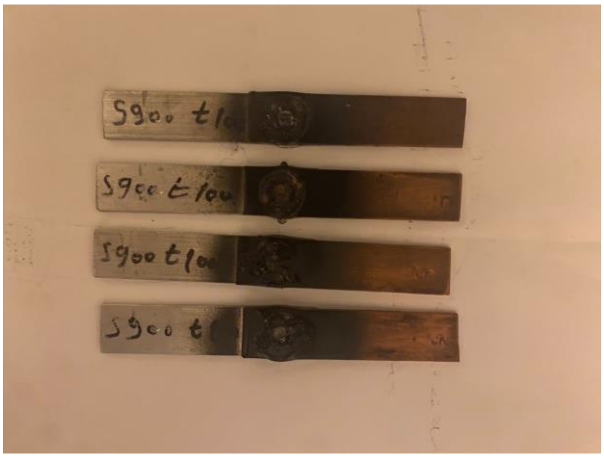

Fig. 2. Macroscopic appearance of representative AA6061-T6/pure Cu lap-shear specimens welded at the optimum FSSW parameters (900 rpm, 100 s, square pin). The keyhole left by the tool pin is visible at the centre of each weld nugget

Table 3. FSSW process parameters and their levels

Parameter	Level 1	Level 2	Level 3
Rotational speed, rpm	900	1450	1800
Dwell time, s	100	120	140
Tool shape	Cylindrical	Square	Hexagonal

Table 4. Taguchi L9 orthogonal array used for FSSW optimization

Run	Rotational speed, rpm	Dwell time, s	Tool shape
L1	900	100	Square
L2	900	120	Hexagonal
L3	900	140	Cylindrical
L4	1450	100	Cylindrical
L5	1450	120	Square
L6	1450	140	Hexagonal
L7	1800	100	Hexagonal
L8	1800	120	Cylindrical
L9	1800	140	Square

Three replicates were welded for each row, and the average maximum tensile-shear load was used as the response variable for the signal-to-noise (S/N) ratio analysis under the larger-the-better criterion [39 – 41]. Each tensile-shear value reported hereafter represents the mean of three nominally identical replicates per condition, so that each value already embeds the averaging of run-to-run scatter inherent to the FSSW process.

The signal-to-noise (S/N) transformation applied throughout the Taguchi analysis is itself a variability-weighted metric, and the factor significance is quantified directly through the ANOVA F-ratios and their associated p-values reported in Section 3.3. The individual replicate readings were archived only as per-condition means rather than as a full per-specimen data set, so explicit standard deviations, confidence intervals and dispersion bands could not be reconstructed for the present manuscript; a fully replicated campaign that retains the per-specimen records, enabling error bars, standard deviations and tighter significance levels, is therefore recommended as the natural quantitative extension of this study.

2.3. Laser shock peening treatment

Laser shock peening was performed on the optimum FSSW joint identified by the Taguchi analysis using a Q-switched Nd: YAG laser (Model J-200, 300 W, 220 V AC, 1 – 10 Hz repetition rate) with a fundamental wavelength of 1064 nm and a pulse duration of 10 ns [42]. A schematic of the laser shock peening setup is shown in Fig. 3. A thin layer of distilled water (≈ 1 mm) was used as the transparent dielectric overlay to confine the laser-induced plasma; no opaque sacrificial coating was applied, in line with the modified-LSP configuration adopted in [30, 42]. The water layer fulfils two complementary roles: it raises the peak plasma pressure by approximately one order of magnitude relative to the open-air configuration, and it suppresses the thermal contribution of the laser–matter interaction by absorbing the radiation from the expanding plasma plume.

The individual LSP parameters were selected on the basis of established laser-peening practice for aluminium alloys rather than arbitrarily. The fundamental Nd: YAG wavelength of 1064 nm was retained because it is efficiently transmitted through the water confinement layer and is strongly coupled to metallic surfaces, maximizing the fraction of pulse energy converted into plasma pressure.

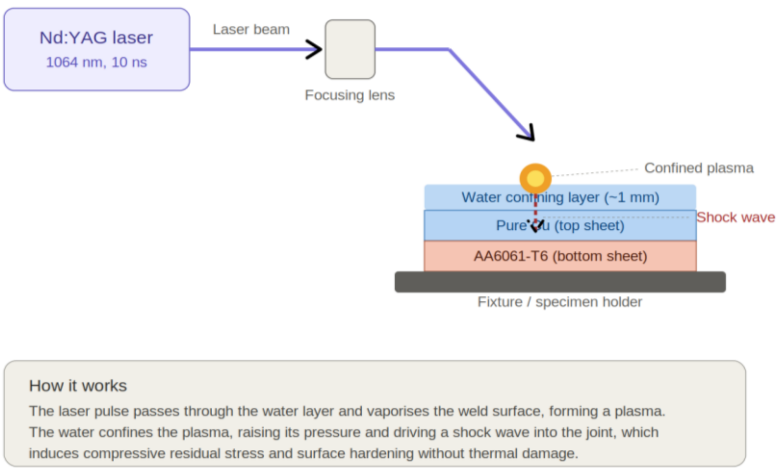

Fig. 3. Schematic of the laser shock peening (LSP)

A nanosecond pulse duration of 10 ns was chosen because, for water-confined LSP, pulses in the few-to-tens-of-nanoseconds range generate a sufficiently long pressure pulse to drive a plastic shock wave deep into the substrate while remaining short enough to keep the process mechanically rather than thermally dominated; this duration is typical of the regime over which compressive residual stresses, rather than surface ablation, are the primary outcome. The 1 – 10 Hz repetition rate was kept low deliberately, so that successive pulses act on a thermally relaxed surface and cumulative heating of the thin lap joint is avoided. The 50 % spot overlap in the raster pattern was selected to ensure full, uniform coverage of the 12 mm nugget footprint, since partial overlap is widely reported to homogenize the surface plastic-strain field and prevent untreated gaps between adjacent impacts.

Finally, the ≈ 1 mm distilled-water overlay was used as the transparent confining medium in preference to an open-air configuration because confinement is the single most influential factor in raising the peak plasma pressure and hence the depth of the compressive layer. These choices collectively place the present treatment within the conventional water-confined, nanosecond LSP regime documented for AA6061 and related alloys [30, 32, 42].

A custom rig was specially designed to fix the FSSW lap-shear specimen and to allow fine vertical and horizontal positioning of the laser handpiece, so that the laser pulses could be directed exclusively to the weld nugget area, minimizing the number of shocks required and avoiding unnecessary irradiation of regions outside the joint. The peening sequence consisted of overlapping pulses arranged in a rectangular raster pattern over the 12 mm diameter nugget footprints, with a nominal spot diameter of 1.5 mm and a 50 % overlap between adjacent spots. Two specimen groups were prepared for the comparative study: as-welded (baseline) and LSP-treated. The laser source was operated at its rated average power of 300 W with a repetition rate in the 1 – 10 Hz range; the spot diameter quoted above is the nominal focusing value. It should be noted, however, that the absolute pulse energy delivered at the specimen surface and the corresponding laser fluence and power density were not determined by direct measurement in the present work, and the effective spot size on the sample was not independently characterized. Consequently, the LSP intensity is reported here only in terms of the nominal machine settings, and quantitative fluence/ablation-threshold values are not claimed. A rigorous characterization of the on-sample spot radius and fluence, for example by the diameter-squared (D^2) versus pulse-energy method of Liu, is recommended in future work to enable precise reproduction and cross-study comparison of the laser–matter interaction conditions.

2.4. Mechanical and microstructural characterization

Lap-shear tensile testing was performed on a WDW-200E universal testing machine of 200 kN capacity at a constant cross-head speed of 1.5 mm min^{-1} at room temperature, in accordance with the ASTM E8M-04 standard. Three samples of each base metal were also tested to provide a reference for the welding-efficiency calculation. The welding efficiency η is defined as [43]:

$$\tau = \frac{F}{A}; \quad (1)$$

$$\eta(\%) = (\tau/UTS_{Cu}) \times 100, \quad (2)$$

where F is the maximum tensile-shear load (N); A is the $\pi(d/2)^2$ = 113.1 mm² is the effective bonded nugget area associated with the 12 mm tool-shoulder diameter, and TS_{Cu} = 220 MPa is the ultimate tensile strength of the weaker base metal (annealed pure copper) [44]. Here Eq. 1 defines the nominal shear stress τ carried by the bonded nugget, and Eq. 2 expresses the welding efficiency η as the ratio of τ to the ultimate tensile strength of the weaker base metal. The efficiency η is referenced to the full tool-shoulder projected area (113.1 mm²) rather than to the true load-bearing bonded area, which is smaller; the reported η values are therefore conservative lower-bound estimates, used on a consistent basis for relative comparison between runs rather than as absolute joint-strength ratios.

Vickers microhardness tests were performed on metallographically polished cross-sections at the mid-thickness of the joint, with a 200 g load and a 10 s dwell time, at a step size of 0.5 mm across the entire welded zone spanning the AA6061-T6 base metal, HAZ, TMAZ, stir zone (SZ), the Al/Cu interface, and the pure Cu base metal. Optical microstructural examination was carried out after etching the aluminum side with Keller's reagent followed by a diluted Poulton's etchant, and the copper side with a ferric-chloride solution.

Surface morphology and elemental distribution were characterized using a field-emission scanning electron microscope (FE-SEM, TESCAN MIRA3) coupled with an EDS detector, operated at 15 – 20 kV with a working distance of 10 mm and at magnifications between 500× and 25 000×. X-ray diffraction (XRD) patterns were collected on a Philips X'Pert (PANalytical, Holland) diffractometer using Cu-Kα radiation (λ = 1.5406 Å) over a 2θ range of 30 – 90° at a step size of 0.02° and a count time of 1 s per step. Surface chemistry was examined by Fourier-transform infrared spectroscopy (FTIR, Shimadzu 8400S) over a wavenumber range of 4000 – 400 cm^{-1} at a resolution of 4 cm^{-1}.

3. RESULTS AND DISCUSSION

3.1. Stacking sequence and joint formation

Prior to the main experimental design, a preliminary investigation evaluated the impact of the material stacking sequence on joint formation [18, 45]. The two configurations were welded using a single set of mid-range parameters (1450 rpm, 120 s, cylindrical pin) selected to obtain a fair comparison between the two stacking arrangements. The results, summarized in Table 5, indicate that the joints failed to form successfully when AA6061-T6 was placed on top of pure copper (maximum load of 1.46 kN with brittle interfacial failure), whereas the copper-on-top configuration produced sound joints reaching 1.89 kN. The Cu-on-top stacking was therefore adopted as the primary configuration for the systematic optimization.

Table 5. Effect of stacking sequence on the tensile-shear performance of FSSW joints

Sample no.	Material configuration	Maximum load, kN
1	AA6061-T6 (top)/pure Cu (bottom)	1.46
2	Pure Cu (top)/AA6061-T6 (bottom)	1.89

This finding agrees with the trend reported by Fuse et al. [18] and Mubiayi and Akinlabi [46] for FSSW Al/Cu, and is rooted in the higher ductility of annealed copper, which permits smoother material flow around the rotating tool pin and effective mechanical interlocking across the lap interface.

3.2. Taguchi optimization of FSSW parameters

The maximum tensile-shear loads measured for the nine L9 runs are summarized in Table 6, together with the corresponding S/N ratios computed using the larger-the-better formulation [39, 41]:

$$\frac{S}{N} = -10 \log 10[(1/n) \cdot \sum(1/y^2)], \qquad (3)$$

where y is the measured tensile-shear load; n is the number of replicates.

Table 6. Maximum tensile-shear load, S/N ratio and welding efficiency for the L9 runs

Run	Max load, kN	τ, MPa	S/N, dB	η, %
L1	3.60	31.83	71.13	14.47
L2	3.24	28.65	70.21	13.02
L3	1.81	16.00	65.15	7.27
L4	3.24	28.65	70.21	13.02
L5	1.32	11.67	62.41	5.31
L6	2.30	20.34	67.23	9.24
L7	2.52	22.28	68.03	10.13
L8	1.73	15.30	64.76	6.95
L9	2.77	24.49	68.85	11.13

Run L1 (900 rpm, 100 s, square pin) yielded the highest load of 3.60 kN and the highest S/N value of 71.13 dB, identifying it as the optimum parameter combination. The lowest performance was observed for L5 (1450 rpm, 120 s, square pin) at 1.32 kN, attributable to insufficient material flow combined with intermediate heat input that promoted the formation of brittle IMC bands without effective mechanical interlocking [20, 47]. The welding efficiency η of the optimum joint was 14.47 %, in line with values reported by [17] for unoptimized FSW Al/Cu pairs of comparable thickness. Fig. 4 displays the experimental shear stress-strain curves for all nine L9 runs, ordered by peak shear strength.

3.3. Analysis of variance

To quantify the relative contribution of each FSSW parameter, an analysis of variance (ANOVA) was performed on the S/N data with a 95 % confidence level [39, 41]. The sum of squares for each factor was calculated as the deviation of its level means from the overall S/N mean, and the percentage contribution was computed as the ratio of each factor's sum of squares to the total sum of squares. The ANOVA results are summarized in Table 7.

Table 7. ANOVA results for the FSSW Taguchi L9 design

Factor	DOF	SS	MS	F-ratio	p-value	Contribution, %
Rotational speed	2	21.45	10.73	13.01	0.071	28.7
Dwell time	2	16.14	8.07	9.78	0.093	21.6
Tool shape	2	33.85	16.93	20.52	0.047	45.3
Error	2	3.29	1.65	–	–	4.4
Total	8	74.73	–	–	–	100.0

Tool shape emerged as the most influential parameter with a contribution of 45.3 %, followed by rotational speed (28.7 %) and dwell time (21.6 %); the residual error accounted for only 4.4 %, confirming the adequacy of the model. The statistical significance of each factor was assessed from its F-ratio against the critical value $F_{0.05}(2, 2) = 19.0$. On this basis, tool shape is statistically significant at the 95 % confidence level ($F = 20.52$, $p = 0.047$), while rotational speed ($p = 0.071$) and dwell time ($p = 0.093$) are significant only at a relaxed $\alpha \approx 0.10$ level. The comparatively high p-values of the latter two factors are a direct consequence of the limited two degrees of freedom available for the pooled error term in an unreplicated L9 layout, rather than an indication of a weak physical effect; their substantial percentage contributions (28.7 % and 21.6 %) confirm that both remain physically meaningful.

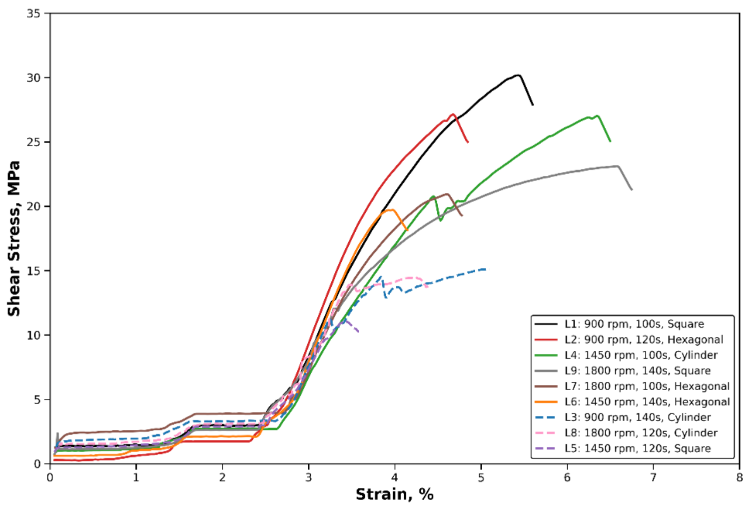

Fig. 4. Experimental shear stress-strain curves for the nine L9 Taguchi-array FSSW joints, ordered by peak shear strength. Run L1 (900 rpm, 100 s, square pin) shows the highest peak shear stress of 31.83 MPa

A confirmatory experimental design with a larger number of error degrees of freedom, for example through additional replicated runs or factor pooling, is recommended in future work to tighten these significance estimates. The dominance of the tool-shape factor is consistent with the trend reported by [25] for FSSW tool-design optimization and by [26] for FSW dissimilar aluminum joints.

The optimum configuration 900 rpm, 100 s and a square pin corresponds to a moderate heat input that is sufficient to plasticize the soft copper top sheet without excessive thermal exposure that would otherwise promote a thick, continuous IMC layer at the Al-Cu interface [20, 47]. The square pin geometry outperformed the cylindrical and hexagonal profiles because of its more effective stirring action: the alternating flat–corner contact generates a pulsed plastic-strain field that enhances material mixing while limiting the residence time of the molten-like material at any single location [25, 26, 48].

3.4. Tensile-shear behavior before and after LSP

The optimum joint (L1) was tested before and after LSP treatment. As summarized in Table 8, the maximum tensile-shear load increased from 3.60 kN in the as-welded condition to 4.20 kN after LSP, a relative improvement of approximately 17 %. Correspondingly, the welding efficiency η rose from 14.47 % to 16.88 %.

Table 8. Tensile-shear performance of the optimum joint before and after LSP

Condition	Max load, kN	η, %
As-welded (Pre-LSP)	3.60	14.47
LSP-treated (Post-LSP)	4.20	16.88

It should be noted that these two percentages are distinct quantities and must not be conflated: the 17 % figure is the relative increase in tensile-shear load produced by LSP (4.20 vs. 3.60 kN), whereas η is the absolute welding efficiency defined in Eq. 2 as the ratio of the nominal shear stress to the ultimate tensile strength of the weaker base metal (220 MPa). The +17 % value reported in Table 8 for comparison with the literature is therefore the LSP-induced load gain, not the welding efficiency η tabulated in Table 6 and Table 9. This improvement is attributed to two coupled mechanisms:

– The introduction of compressive residual stresses in the surface layer, which according to the established literature on LSP [49, 50] is expected to retard crack initiation and slow near-surface crack growth under cyclic loading, although no fatigue testing was performed in the present work and this effect remains to be confirmed for the specific Al/Cu dissimilar joint [49, 50].
– The strain-hardening of the near-surface region under the rapid LSP loading, which increases the energy required for plastic instability [32].

Comparable post-LSP load increments (10 – 25 %) have been reported for similar-metal FSW aluminum joints by Hatamleh et al., the present 17 % gain is consistent with the 10 – 25 % increments reported by Hatamleh et al. [33, 34] and Balos et al. [36]. Those studies, however, concerned similar-metal aluminium FSW joints that respond uniformly to peening, whereas the present dissimilar AA6061-T6/pure Cu joint responds asymmetrically, the aluminium strengthens while the copper softens. Achieving a net 17 % gain despite this copper softening shows that the strengthening of the aluminium HAZ governs the joint response, a distinction not captured by the single-alloy studies above [33, 34] and Balos et al. [36]. The corresponding lap-shear specimens after tensile-shear testing, showing the typical interfacial-shear failure mode at the Al/Cu nugget periphery, are presented in Fig. 5.

To place this result in context, Table 9 provides a quantitative comparison of the present findings with selected published studies on post-weld surface treatment of FSW aluminium and dissimilar Al-based joints. The present 17 % tensile-shear gain and 27 % hardness recovery on the Al side are consistent with the range of improvements reported in the literature, while the simultaneous copper softening is a feature unique to the dissimilar Al/Cu system investigated here.

a

b

c

Fig. 5. Three representative AA6061-T6/pure Cu lap-shear specimens after tensile-shear testing, showing the typical interfacial-shear failure mode at the Al/Cu nugget periphery for the optimum FSSW joint

Table 9. Quantitative comparison of LSP/post-weld treatment effects on FSW Al-based joints reported in the literature. The +17 % value listed for the present work is the relative LSP-induced gain in tensile-shear load, not the welding efficiency η reported in Table 6 and Table 8

Study	Material/Joint	Treatment	Key result	Ref.
Hatamleh et al. (2007)	AA7075-T7351 FSW	LSP	~10× reduction in fatigue crack growth rate	[33]
Balos et al. (2025)	AW6060 bobbin-tool FSW	LSP	Significant HAZ hardness increase; ~15–20 % gain	[36]
Su et al. (2016)	AA6061 welded joints	LSP	Enhanced fatigue life; compressive residual stress introduced	[37]
Kashaev et al. (2020)	AA6056 laser beam-welded	LSP	Retardation of surface fatigue crack propagation	[28]
Present work	AA6061-T6 / Pure Cu FSSW (dissimilar)	LSP (post-FSSW)	+17 % tensile-shear load; +27 % Al hardness; asymmetric Cu softening	–

3.5. Microhardness profile

Vickers microhardness profiles measured across the joint cross-section before and after LSP are illustrated in Fig. 6. In the as-welded condition, the Aluminum side exhibited the double-minimum hardness distribution previously reported for FSW joints of AA6061-T6 [51, 52]: a base-metal hardness of 64.32 HV decreased to a localized minimum of 60.67 HV in the HAZ, recovered to ≈ 65 HV in the thermo-mechanically affected zone (TMAZ), and rose to a peak of 86 HV at the stir-zone interface. The HAZ softening is unequivocally attributed to the dissolution and over-ageing of the strengthening β-Mg_2Si precipitates during the welding thermal cycle, which removes the principal precipitation-hardening contribution of the T6 temper [52]. The pure copper side maintained a stable hardness of approximately 78.76 HV with a peak of ≈ 92 HV at the SZ interface, the latter resulting from grain refinement and the local presence of $CuAl_2$ and Cu_9Al_4 intermetallic [43].

After LSP treatment, the hardness profile underwent a pronounced transformation. On the aluminum side, the base-metal hardness rose to 81.70 HV an increase of 27 % and the previously softened HAZ recovered to 77.62 HV, exceeding the original base-metal value. The SZ peak hardness on the aluminum side increased from 86 HV to 92 HV. This enhancement is governed by Taylor hardening through dislocation proliferation and Hall-Petch grain refinement, both induced by the severe near-surface straining imposed by the laser-generated pressure pulses [32, 34]. Importantly, the LSP-induced gain on the Al side fully compensates for the welding-induced HAZ loss, restoring and exceeding the pristine T6 hardness without re-applying a heat treatment.

The pure copper side, however, exhibited an opposite, lower-magnitude response: the base-metal hardness decreased from 78.76 HV to 69.12 HV. This behavior is attributed to laser-induced thermal recovery, a mechanism consistent with the well-documented thermophysical properties of pure copper. Pure copper combines an exceptionally high thermal conductivity (≈ 401 W m^{-1} K^{-1}), a low recrystallization temperature (≈ 200 °C for cold-worked Cu) and high stacking-fault energy, all of which favor rapid dislocation annihilation and recovery over strain hardening under transient thermal loading.

As a result, the rapid plasma-energy absorption at the Cu surface, although shorter than 100 ns per pulse, is dissipated into the bulk fast enough to trigger localized recovery and partial recrystallization of the dislocations introduced both by the prior FSSW and by the LSP itself, outweighing the mechanical hardening contribution.

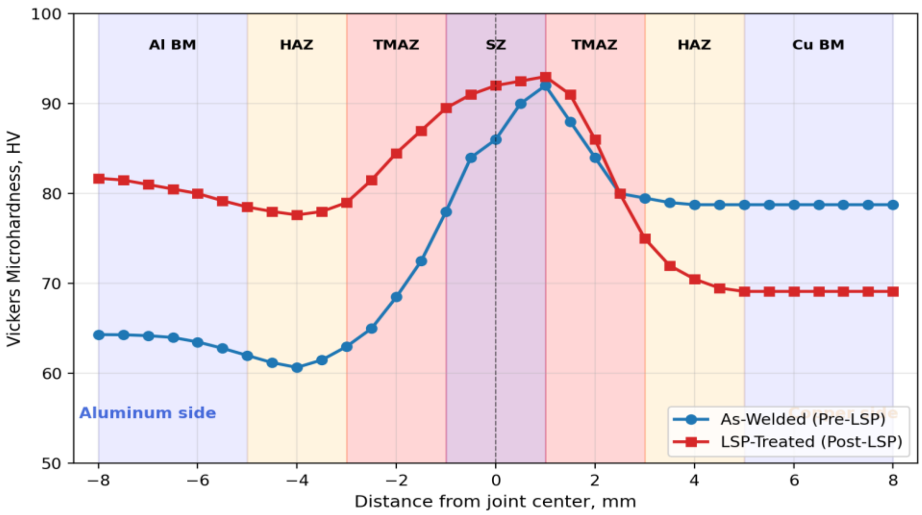

Fig. 6. Vickers microhardness profiles measured across the AA6061-T6/pure Cu FSSW joint cross-section before (As-welded) and after (LSP-treated) the laser shock peening treatment. The aluminum side exhibits a dual-minimum hardness profile with HAZ softening recovered after LSP, while the copper side shows a moderate thermal-recovery softening after LSP

This thermal-relaxation mechanism in LSP-treated copper is consistent with the observations of Cao et al. [53], who reported analogous softening in LSP-processed copper substrates, and with the general framework of Montross et al. [32], who noted that materials with high thermal diffusivity may not retain the full LSP-induced dislocation substructure. It is acknowledged that direct microstructural verification, for example by EBSD mapping of grain-boundary character or TEM dislocation-density quantification before and after LSP, would confirm this interpretation, and is recommended as future work.

The asymmetric LSP response, strengthening on the AA6061-T6 side and moderate softening on the Cu side, is the central metallurgical finding of the present work. From an engineering standpoint, the net effect is still beneficial because the limiting partner in the joint is the precipitation-hardenable aluminum HAZ, where the welding thermal cycle removes the strengthening phases. By targeting the LSP application to the Al face, the welding-induced softening can be compensated without re-introducing a high-temperature ageing step, which is impractical for thin-walled assemblies and for joints already containing a stable IMC band.

3.6. Microstructural evolution

Optical microscopy of the as-welded cross-section revealed the four characteristic FSW zones: base metal (BM), HAZ, TMAZ, and stir zone (SZ). The AA6061-T6 BM showed elongated α-Al grains aligned in the rolling direction with dispersed alloying precipitates; the Pure Cu BM exhibited homogeneous equiaxed grains with random crystallographic orientations and the typical contrast variation under polarized light (Fig. 7). The HAZ on the Al side displayed coarsened grains consistent with the over-ageing of the β-Mg_2Si precipitates that drives the hardness minimum reported in Section 3.5. The TMAZ exhibited the typical bent and partially recrystallized grain structure produced by the combined thermal and mechanical action of the rotating tool. In the SZ, the high-temperature, high-shear plastic deformation produced a fine equiaxed dynamically recrystallized grain structure on the Al side, intermixed with elongated Cu fragments swept from the top sheet, in agreement with the microstructural mechanism proposed by [46]. The present study did not include a quantitative characterization of the Al-Cu intermetallic layer; the interfacial morphology is described here only on the basis of optical and secondary-electron imaging. Quantitative EDS elemental mapping and line-scan analysis across the Al/Cu interface, together with measurement of the IMC-layer thickness before and after LSP, are planned as future work to correlate the interfacial chemistry directly with the mechanical response.

After LSP, the topmost surface layer of both sheets showed a high-density slip-band morphology and additional grain refinement consistent with the severe surface plastic flow imposed by the laser-induced pressure pulses.

SEM imaging of the LSP-treated surfaces (Fig. 8) confirmed surface densification, the formation of distinct slip bands, and the closure of pre-existing micro-voids on both metals. On the Al side, the grain-refined layer extended approximately 50 – 100 µm into the bulk, consistent with the depth at which the shock-wave pressure remains above the dynamic yield strength of AA6061-T6. On the Cu side, a similar morphology was observed near the surface but coexisted with regions of partial annealing, supporting the thermal-recovery mechanism inferred from the hardness data.

3.7. X-ray diffraction analysis

XRD patterns of the pure Cu and AA6061-T6 specimens, in the as-welded and LSP-treated conditions, are shown in Fig. 9. The as-welded patterns showed sharp, intense peaks at $2\theta \approx 43.4°$, 50.5° and 74.1° for the (111), (200) and (220) FCC-Cu planes, and at $2\theta \approx 38.62°$, 44.87°, 65.1° and 78.2° for the (111), (200), (220) and (311) FCC-Al planes, indicating coarse-grained, low-strain starting microstructures. The Cu pattern additionally exhibited a weak reflection at $2\theta \approx 36.5°$, assigned to the (111) plane of cuprous oxide (Cu_2O), consistent with the thin surface-oxide layer subsequently confirmed by the Cu-O band in the FTIR spectra (Section 3.8).

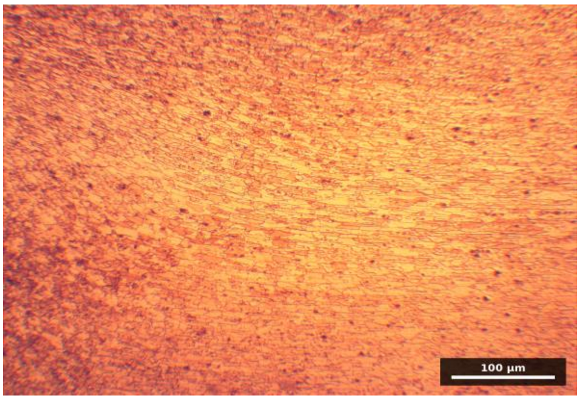

a

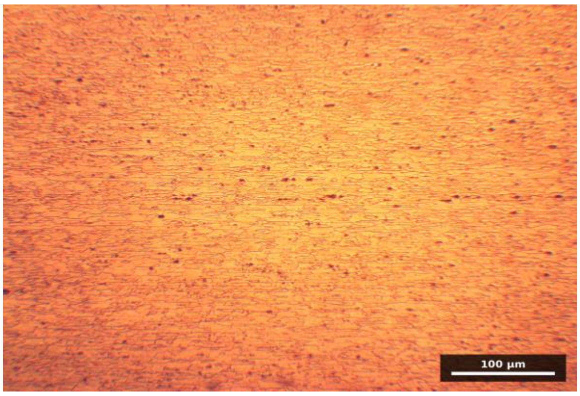

b

Fig. 7. Optical microstructure of the as-welded dissimilar AA6061-T6/pure Cu FSSW joint (etched): a – AA6061-T6 stir-zone region showing dynamically recrystallized fine α-Al grains; b – pure Cu base-metal region showing equiaxed grains with annealing twins

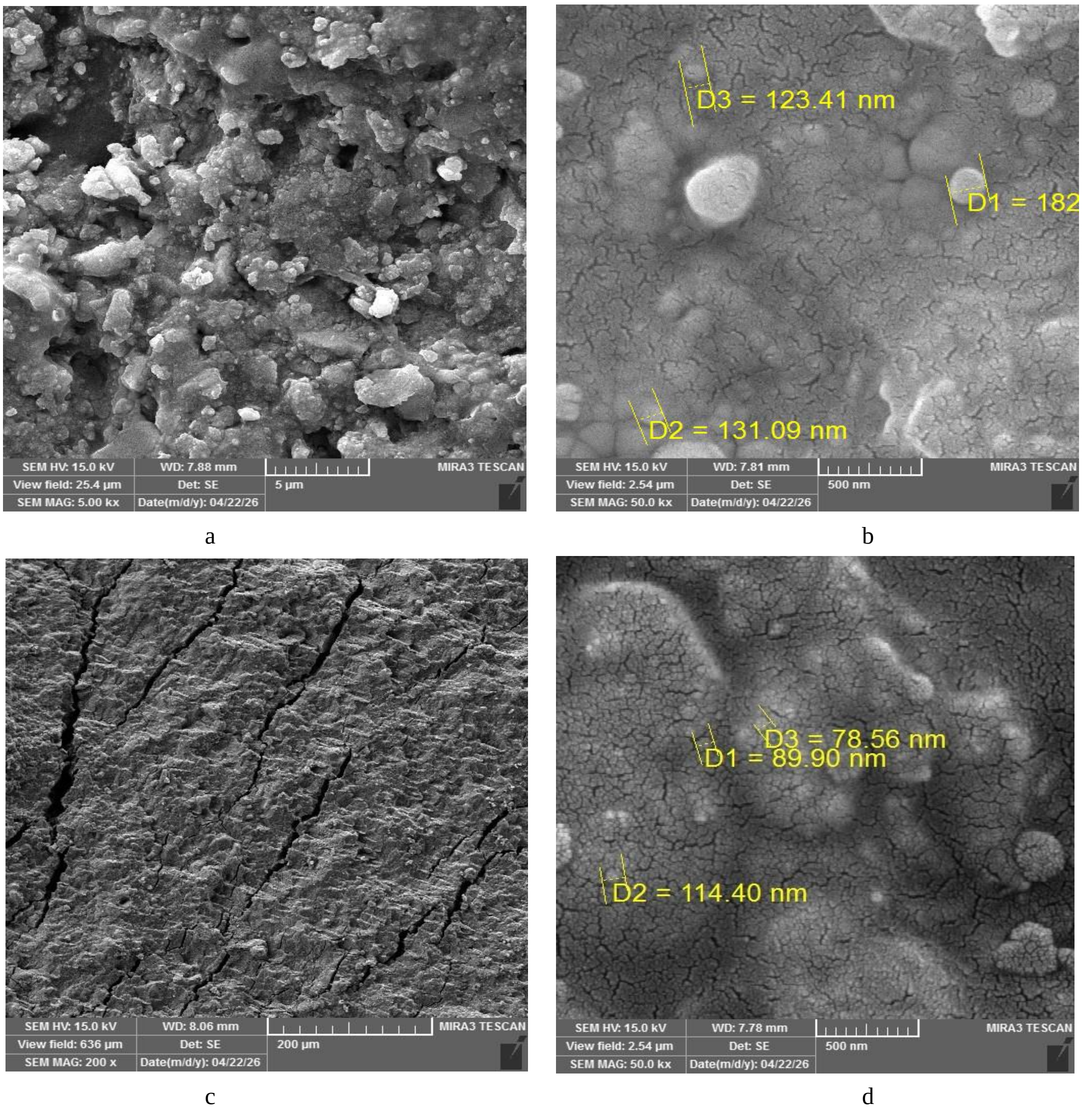

Fig. 8. FE-SEM Micrographs of the joint surfaces: a, b – pure Cu surface in the as-welded and LSP-treated conditions, respectively, showing surface densification and grain-boundary refinement after LSP; c, d – AA6061-T6 surface in the as-welded and LSP-treated conditions, respectively, showing distinct slip-band morphology and surface flattening after LSP

After LSP, two consistent changes were observed. First, all main diffraction peaks of both metals broadened: the full-width at half-maximum (FWHM) of the Cu (200) plane increased from 0.19° to 0.246°, and an analogous broadening was observed on the Al (111) and (200) planes. Peak broadening is the diffraction-level signature of grain refinement and an increase in dislocation density, and is the expected response to the intense near-surface straining associated with LSP [32, 50]. Second, the Al (111) peak shifted from 38.62° to 38.68° – a shift of +0.06° toward higher angles, which by Bragg's law corresponds to a contraction of the interplanar spacing and is a recognized indirect indicator of compressive residual stress development in the surface layer [50].

The combined XRD response peak broadening plus a positive 2θ shift on the Al side is fully consistent with the dual hardening mechanism proposed in Section 3.5 (Taylor + Hall–Petch on the Al side) and provides crystallographic-level support for the mechanical hardness data. On the Cu side, the broadening was the dominant feature, while the angular shift was negligible – in line with the proposed thermal recovery, in which the dislocation cells introduced by LSP partially rearrange and the residual-stress build-up is suppressed. From a quantitative standpoint, the FWHM ratio (LSP/as-welded) of 1.30 observed on the Cu (200) plane is broadly consistent with the values reported for LSP of similar-metal Cu by [53], suggesting that the dislocation-multiplication mechanism is universal across Cu substrates while the subsequent thermal evolution is dictated by the local conduction conditions.

The peak broadening can also be read in terms of the classical Williamson-Hall framework, which separates the total broadening into a grain-size contribution and a lattice-microstrain contribution. The simultaneous broadening of the (111) and (200) Al peaks observed here implies that both size refinement and lattice micro-strain contribute to the LSP response, in proportions that cannot be reliably separated from a two-peak data set. This dual contribution is consistent with the dynamic deformation regime of LSP and underlines the value of complementing the present static characterization with future TEM dislocation-density measurements.

3.8. FTIR surface chemistry

FTIR spectroscopy was used to determine whether LSP induced detectable thermal oxidation of the joint surfaces. Across all four specimens, as-welded Cu, LSP-Cu, as-welded Al, and LSP-Al (Fig. 10), a broad absorption band at 3420 – 3450 cm⁻¹ corresponded to the O-H stretching of adsorbed moisture, and a band at 1630 – 1640 cm⁻¹ corresponded to the H-O-H bending of molecular water, both expected for laboratory-handled metal surfaces and of no diagnostic value for oxidation damage. Two further bands were diagnostic: at 620 – 640 cm⁻¹ (Al-O stretching, indicative of Al_2O_3) and at 530 – 550 cm⁻¹ (Cu-O stretching, indicative of Cu_2O/CuO). The peak assignments are summarized in Table 10.

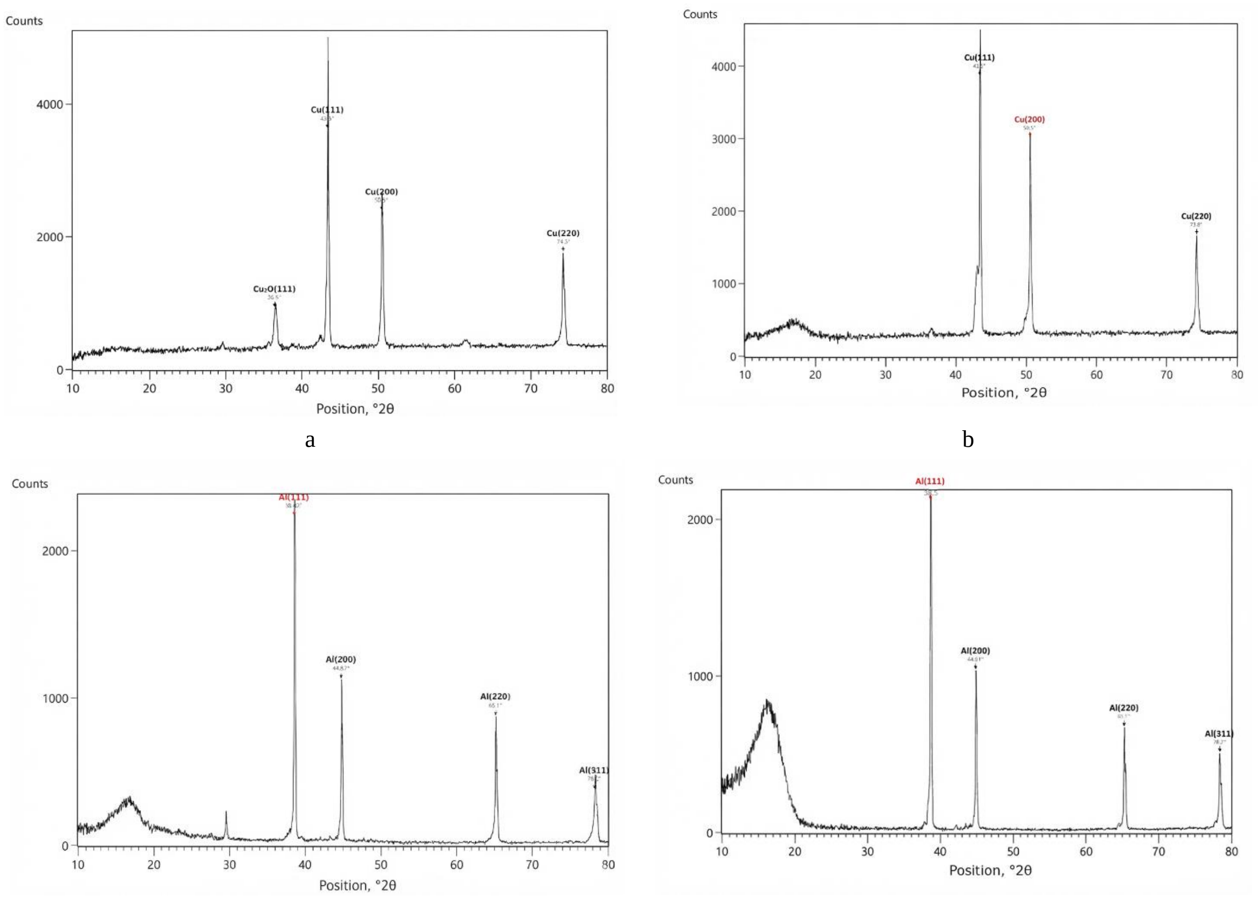

Fig. 9. X-ray diffraction patterns: a, b – pure Cu in the as-welded and LSP-treated conditions, respectively, showing peak broadening on the Cu (200) plane after LSP; c, d – AA6061-T6 in the as-welded and LSP-treated conditions, respectively, showing peak broadening and a positive 2θ shift on the Al (111) plane after LSP

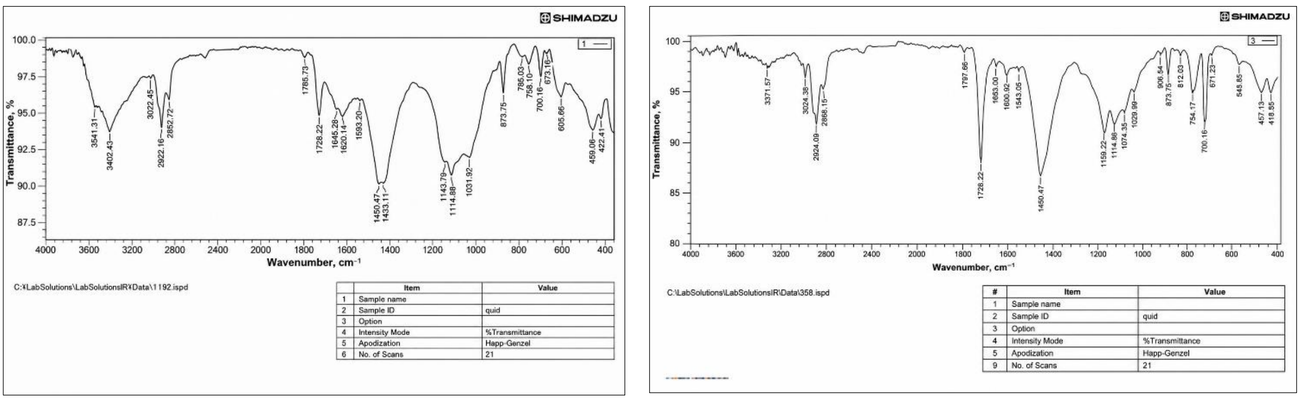

a

b

continues on the next page

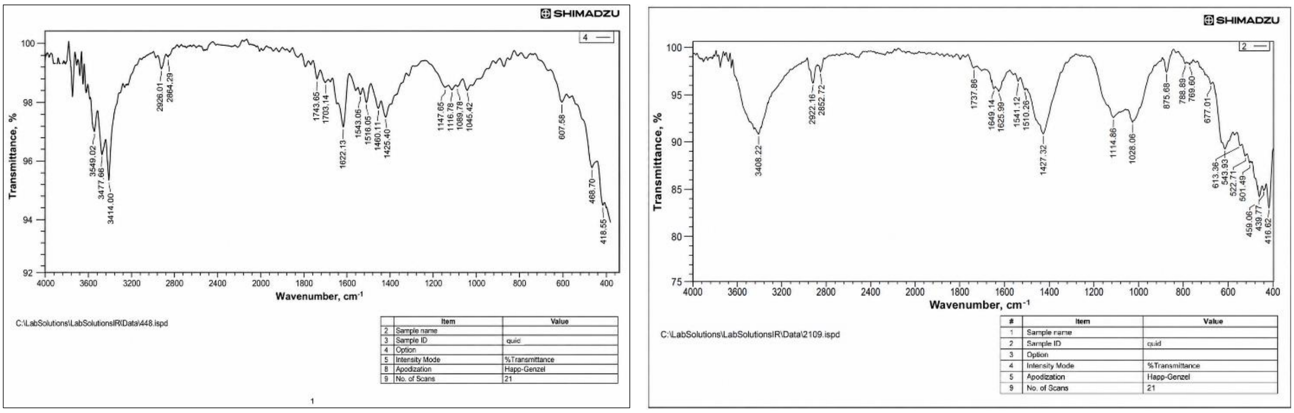

c d

Fig. 10. FTIR transmittance spectra of the four specimens: a – as-welded pure Cu; b – LSP-treated pure Cu; c – as-welded AA6061-T6; d – LSP-treated AA6061-T6. Diagnostic Cu-O (≈ 540 cm^{-1}) and Al-O (≈ 630 cm^{-1}) bands persist with comparable intensities before and after LSP, confirming the absence of significant thermal-oxidation damage

Table 10. FTIR peak positions and assignments for the Al-Cu joints

Wavenumber, cm^{-1}	Functional group	Interpretation
3420 – 3450	O-H stretching	Adsorbed moisture/hydroxyl
1630 – 1640	H-O-H bending	Molecular water absorption
620 – 640	Al-O stretching	Al_2O_3 formation
530 – 550	Cu-O stretching	Cu_2O/CuO formation

The Al-O and Cu-O bands were detected on both as-welded and LSP-treated specimens with comparable intensities, indicating that LSP performed under the dielectric water layer did not induce significant thermal oxidation. Rather, it preserved the thin native oxide film that pre-existed on each base metal and may have densified it slightly, consistent with the surface-densification effect observed by SEM. This is an important engineering finding: in contrast with thermal post-weld treatments, LSP achieves residual-stress and hardness modification without compromising the surface chemistry of either metal a property that is particularly valuable for electrical Al/Cu joints, where surface oxide growth is detrimental to contact resistance. Combined with the densification of the surface micro-asperities documented by SEM, this property suggests that LSP-treated FSSW Al/Cu joints may also offer improved galvanic-corrosion resistance, although this hypothesis remains to be confirmed by direct electrochemical testing in service-relevant electrolytes [54, 55].

These surface-chemistry results also have a direct bearing on the electrical performance of the joint, which is the primary motivation for dissimilar Al-Cu assemblies. The electrical reliability of an Al-Cu interconnect is governed by two distinct resistive contributions: the interfacial IMC band and the surface oxide film. The Al-Cu intermetallic that form at the lap interface are intrinsically poor conductors, the reported room-temperature resistivity of $CuAl_2$ (θ phase) and Cu_9Al_4 (γ_2 phase) lies in the range of ≈ 6 – 13 μΩ cm, roughly four to eight times that of pure copper (≈ 1.7 μΩ cm) and several times that of AA6061 (≈ 4 μΩ cm). A thick, continuous IMC band therefore raises the through-joint contact resistance and degrades the current-carrying capability of the connection. In the present work, the moderate heat input associated with the optimum FSSW condition (900 rpm, 100 s, square pin) was selected precisely to limit the thickness and continuity of this IMC band, which is beneficial not only mechanically but also electrically. The subsequent LSP step, performed under a water confinement layer, does not add an electrically harmful surface oxide: the FTIR spectra show that the native Al_2O_3 and Cu_2O films are preserved rather than thickened, in contrast with thermal post-weld treatments that grow resistive oxide scales. It is emphasized, however, that the present study did not include direct four-point or contact-resistance measurements; the electrical implications are inferred here from the IMC and oxide characterization only, and a dedicated electrical-resistivity and contact-resistance evaluation of the LSP-treated FSSW Al/Cu joint is recommended as future work.

4. CONCLUSIONS

1. The Cu-on-top stacking sequence was essential to produce sound dissimilar AA6061-T6 / Pure Cu FSSW joints. Taguchi L9 optimization with ANOVA identified tool shape as the most influential parameter (45.3 % contribution), ahead of rotational speed and dwell time; the optimum condition (900 rpm, 100 s, square pin) gave a maximum tensile-shear load of 3.60 kN.
2. LSP produced an asymmetric hardness response: the Aluminum side fully recovered its welding-induced HAZ softening and exceeded its base-metal hardness (about +27 %) through Taylor hardening and Hall-Petch refinement, whereas the copper side softened moderately by laser-induced thermal recovery. Despite this asymmetry, the optimum joint showed a net macroscopic strengthening, its tensile-shear load rising by 17 % (from 3.60 to 4.20 kN), confirming that the response of the precipitation-hardenable Al HAZ governs the joint behaviour.

3. XRD supported these mechanical trends: peak broadening on both metals indicated grain refinement and higher dislocation density, while a small positive shift of the Al (111) peak was consistent with surface compressive lattice strain. FTIR confirmed that LSP, performed under a water overlay, introduced no thermal-oxidation damage, the native Cu_2O and Al_2O_3 surface bands persisting with comparable intensities before and after treatment.
4. The integrated FSSW + LSP route is therefore proposed as a viable post-weld strengthening strategy for thick (3 mm) dissimilar AA6061-T6/pure Cu lap joints in electrical, automotive, and aerospace applications. The surface compressive strain inferred here from the XRD response was not measured directly; its quantification by the X-ray $\sin^2\psi$ method, hole-drilling or neutron diffraction, together with fatigue-life validation under cyclic loading, is recommended as the natural extension of this static-loading study.

Acknowledgments

The authors gratefully acknowledge the Department of Metallurgy and Materials Engineering, Faculty of Engineering, Karabük University (Türkiye) for the laboratory facilities, and the staff of Sharif University of Technology (Tehran, Iran) and Kashan University (Iran) for assistance with the SEM/EDS and XRD measurements, respectively.

REFERENCES

1. **Callister, Jr.W.D., Rethwisch, D.G.** Materials Science and Engineering: An Introduction. John Wiley & Sons, 2020.
2. **Meng, Q., Wang, C.H., Saber, N., Kuan, H.C., Dai, J., Friedrich, K., Ma, J.** Nanosilica-Toughened Polymer Adhesives *Materials & Design* 61 2014: pp. 75 – 86. https://doi.org/10.1016/j.matdes.2014.04.042
3. **Salvador, D.C.** Comparative Study of Welding Techniques for Joining Dissimilar Metals *International Journal of Advanced Research in Science, Communication and Technology* 3 (1) 2023: pp. 988 – 992. https://doi.org/10.48175/IJARSCT-11903
4. **Srinivasan, D., Subramanian, P.** Kirkendall Porosity During Thermal Treatment of Mo–Cu Nanomultilayers *Materials Science and Engineering: A* 459 (1 – 2) 2007: pp. 145 – 150. https://doi.org/10.1016/j.msea.2007.01.037
5. **Fang, Y., Jiang, X., Mo, D., Zhu, D., Luo, Z.** A Review on Dissimilar Metals' Welding Methods and Mechanisms with Interlayer *The International Journal of Advanced Manufacturing Technology* 102 2019: pp. 2845 – 2863. https://doi.org/10.1007/s00170-019-03353-6
6. **Mishra, R.S., Ma, Z.Y.** Friction Stir Welding and Processing *Materials Science and Engineering: R: Reports* 50 (1 – 2) 2005: pp. 1 – 78. https://doi.org/10.1016/j.mser.2005.07.001
7. **Sarsilmaz, F., Gürocak Çelik, B.** Microstructural and Numerical Variation of Friction Spot Welded AA7075 Couples *Materials Testing* 65 (9) 2023: pp. 1373 – 1381. https://doi.org/10.1515/mt-2023-0142
8. **Mishra, A.** Friction Stir Welding of Dissimilar Metal: A Review *International Journal for Research in Applied Science & Engineering Technology* 2018: p. 12. https://dx.doi.org/10.2139/ssrn.3104223
9. **Boumerzoug, Z.** Joining of Dissimilar Materials by Friction Stir Welding *MATEC Web of Conferences* 224 2018: p. 01118. https://doi.org/10.1051/matecconf/201822401118
10. **Zhi-Hong, F., Di-Qiu, H., Hong, W.** Friction Stir Welding of Aluminum Alloys *Journal of Wuhan University of Technology* 19 2004: pp. 61 – 64. https://doi.org/10.1007/BF02838366
11. **Kumar, H.A., Ramana, V.V.** An Overview of Friction Stir Welding (FSW): A New Perspective *International Journal of Engineering and Science* 4 (6) 2014: pp. 1 – 4.
12. **Tanaka, T., Morishige, T., Hirata, T.** Comprehensive Analysis of Joint Strength for Dissimilar Friction Stir Welds of Mild Steel to Aluminum Alloys *Scripta Materialia* 61 (7) 2009: pp. 756 – 759. https://doi.org/10.1016/j.scriptamat.2009.06.022
13. **Sato, Y.S., Kokawa, H., Enomoto, M., Jogan, S.** Microstructural Evolution of 6063 Aluminum During Friction-Stir Welding *Metallurgical and Materials Transactions A* 30 (9) 1999: pp. 2429 – 2437. https://doi.org/10.1007/s11661-999-0251-1
14. **Liu, X., Wang, Q., Pei, X., Li, Y., Zhen, Y., Shen, Z., Chen, H.** Microstructural Evolution of 6061-T6 Aluminum Alloy in Vortex-Friction Stir Welding *Materials Characterization* 195 2023: pp. 112544. https://doi.org/10.1016/j.matchar.2022.112544
15. **Hsieh, M.J., Lee, R.T., Chiou, Y.C.** Friction Stir Spot Fusion Welding of Low-Carbon Steel to Aluminum Alloy *Journal of Materials Processing Technology* 240 2017: pp. 118 – 125. https://doi.org/10.1016/j.jmatprotec.2016.08.034
16. **Vaneghi, A.H., Bagheri, B., Shamsipur, A., Mirsalehi, S.E., Abdollahzadeh, A.** Investigations into the Formation of Intermetallic Compounds During Pinless Friction Stir Spot Welding of AA2024-Zn-Pure Copper Dissimilar Joints *Welding in the World* 66 2022: pp. 2351 – 2369. https://doi.org/10.1007/s40194-022-01366-6
17. **Habba, M.I., Ahmed, M.M.** Friction Stir Welding of Dissimilar Aluminum and Copper Alloys: A Review of Strategies for Enhancing Joint Quality *Journal of Advanced Joining Processes* 11 2025: p. 100293. https://doi.org/10.1016/j.jajp.2025.100293
18. **Fuse, K., Badheka, V., Oza, A.D., Prakash, C., Buddhi, D., Dixit, S., Vatin, N.** Microstructure and Mechanical Properties Analysis of Al/Cu Dissimilar Alloys Joining by Using Conventional and Bobbin Tool Friction Stir Welding *Materials* 15 (15) 2022: p. 5159. https://doi.org/10.3390/ma15155159
19. **Mao, Y., Ni, Y., Xiao, X., Qin, D., Fu, L.** Microstructural Characterization and Mechanical Properties of Micro Friction Stir Welded Dissimilar Al/Cu Ultra-Thin Sheets *Journal of Manufacturing Processes* 60 2020: pp. 356 – 365. https://doi.org/10.1016/j.jmapro.2020.10.064
20. **Carlone, P., Astarita, A., Palazzo, G.S., Paradiso, V., Squillace, A.** Microstructural Aspects in Al–Cu Dissimilar Joining by FSW *The International Journal of Advanced Manufacturing Technology* 79 2015: pp. 1109 – 1116. https://doi.org/10.1007/s00170-015-6874-z
21. **Jain, S., Mishra, R., Mehdi, H., Gupta, R., Dubey, A.K.** Optimization of Processing Variables of Friction Stir Welded Dissimilar Composite Joints of AA6061 and AA7075 Using Response Surface Methodology *Journal of Adhesion Science and Technology* 38 (6) 2024: pp. 949 – 968.

https://doi.org/10.1080/01694243.2023.2243682

22. **Manickam, S., Rajendran, C., Nathan, S.R., Sivamaran, V., Balasubramanian, V.** Assessment of the Influence of FSSW Parameters on Shear Strength of Dissimilar Materials Joint (AA6061/AZ31B) *International Journal of Lightweight Materials and Manufacture* 6 (1) 2023: pp. 33 – 45. https://doi.org/10.1016/j.ijlmm.2022.07.005
23. **Avettand-Fènoël, M.N., Nagaoka, T., Marinova, M., Taillard, R.** Upon the Effect of Zn During Friction Stir Welding of Aluminum-Copper and Aluminum-Brass Systems *Journal of Manufacturing Processes* 58 2020: pp. 259 – 278. https://doi.org/10.1016/j.jmapro.2020.08.006
24. **Ahmed, M.M., Touileb, K., El-Sayed Seleman, M.M., Albaijan, I., Habba, M.I.** Bobbin Tool Friction Stir Welding of Aluminum: Parameters Optimization Using Taguchi Experimental Design *Materials* 15 (8) 2022: p. 2771. https://doi.org/10.3390/ma15082771
25. **Arumugam, A., Basak, A.K., Pramanik, A., Littlefair, G.** Tool Geometries and Design of Friction Stir Spot Welding (FSSW) Tools and Effect on Weld Properties – A Comprehensive Review *Materials* 18 (14) 2025: p. 3248. https://doi.org/10.3390/ma18143248
26. **Kumar, P.S., Chander, M.S.** Effect of Tool Pin Geometry on FSW Dissimilar Aluminum Alloys-(AA5083 & AA6061) *Materials Today: Proceedings* 39 2021: pp. 472 – 477. https://doi.org/10.1016/j.matpr.2020.08.204
27. **Arredondo Bravo, M.G., Gomez-Rosas, G., Morales, M., Munoz-Martin, D., Moreno Labella, J.J., Lopez Lopez, J.M., Quiñones Galvan, J.G., Rubio-Gonzalez, C., Casillas Rodriguez, F.J., Molpeceres, C.** Effects of Laser Shock Processing on the Mechanical Properties of 6061-T6 Aluminium Alloy Using Nanosecond and Picosecond Laser Pulses *Materials* 18 (20) 2025: p. 4649. https://doi.org/10.3390/ma18204649
28. **Kashaev, N., Ushmaev, D., Ventzke, V., Klusemann, B., Fomin, F.** On the Application of Laser Shock Peening for Retardation of Surface Fatigue Cracks in Laser Beam-Welded AA6056 *Fatigue & Fracture of Engineering Materials & Structures* 43 (7) 2020: pp. 1500 – 1513. https://doi.org/10.1111/ffe.13226
29. **Kumar, G.V., Rao, C., Selvaraj, N., Bhagyashekar, M.** Studies on Al6061-SiC and Al7075-Al2O3 Metal Matrix Composites *Journal of Minerals & Materials Characterization & Engineering* 9 (1) 2010: pp. 43 – 55.
30. **Gujba, A.K., Medraj, M.** Laser Peening Process and Its Impact on Materials Properties in Comparison with Shot Peening and Ultrasonic Impact Peening *Materials* 7 (12) 2014: pp. 7925 – 7974. https://doi.org/10.3390/ma7127925
31. **Shojaeefard, M.H., Behnagh, R.A., Akbari, M., Givi, M.K.B., Farhani, F.** Modelling and Pareto Optimization of Mechanical Properties of Friction Stir Welded AA7075/AA5083 Butt Joints Using Neural Network and Particle Swarm Algorithm *Materials & Design* 44 2013: pp. 190 – 198. https://doi.org/10.1016/j.matdes.2012.07.025
32. **Montross, C.S., Wei, T., Ye, L., Clark, G., Mai, Y.W.** Laser Shock Processing: A Review of the Physics and Applications. *International Journal of Fatigue* 24 (10) 2002: pp. 1021 – 1036. https://doi.org/10.1016/S0142-1123(02)00022-1
33. **Hatamleh, O., Lyons, J., Forman, R.** Laser and Shot Peening Effects on Fatigue Crack Growth in Friction Stir Welded 7075-T7351 Aluminum Alloy Joints *International Journal of Fatigue* 29 (3) 2007: pp. 421 – 434. https://doi.org/10.1016/j.ijfatigue.2006.05.007
34. **Hatamleh, O., Hackel, L., Forth, S.** Effects of Different R Ratios on Fatigue Crack Growth in Laser Peened Friction Stir Welds *Materials Science Forum* 580 – 582 2008: pp. 675 – 680. https://doi.org/10.4028/www.scientific.net/MSF.580-582.675
35. **Rubio-González, C., Felix-Martinez, C., Gomez-Rosas, G., Ocaña, J., Morales, M., Porro, J.** Effect of Laser Shock Processing on Fatigue Crack Growth of Duplex Stainless-Steel *Materials Science and Engineering: A* 528 (3) 2011: pp. 914 – 919. https://doi.org/10.1016/j.msea.2010.10.020
36. **Balos, S., Pecanac, M., Rajnovic, D., Barenyi, I., Chochlikova, H., Zlatanovic, D.L., Bergmann, J.P., Knezev, M., Radisic, S., Majerik, J.** Influence of Laser Shock Peening on the Bobbin Tool Friction Stir-Welded AW6060 Alloy *Materials* 18 (2) 2025: p. 247. https://doi.org/10.3390/ma18020247
37. **Su, C., Zhou, J., Meng, X., Huang, S.** Improvement in Fatigue Performance of Aluminium Alloy Welded Joints by Laser Shock Peening in a Dynamic Strain Aging Temperature Regime *Materials* 9 (10) 2016: p. 799. https://doi.org/10.3390/ma9100799
38. **Li, S., Wu, X.** Microstructural Evolution and Corresponding Property Changes After Deep Cryotreatment of Tool Steel *Materials Science and Technology* 31 (15) 2015: pp. 1867 – 1878. https://doi.org/10.1179/1743284715Y.0000000038
39. **Montgomery, D.C.** Design and Analysis of Experiments. John Wiley & Sons, 2017.
40. **Roy, R.K., Sarkar, K.** A Primer on the Taguchi Method. Society of Manufacturing Engineers, 2010.
41. **Taguchi, G., Chowdhury, S., Wu, Y.** Taguchi's Quality Engineering Handbook. Wiley, 2004.
42. **Peyre, P., Fabbro, R.** Laser Shock Processing: A Review of the Physics and Applications *Optical and Quantum Electronics* 27 (12) 1995: pp. 1213 – 1229. https://doi.org/10.1007/BF00326477
43. **Xue, P., Xiao, B., Ni, D., Ma, Z.** Enhanced Mechanical Properties of Friction Stir Welded Dissimilar Al–Cu Joint by Intermetallic Compounds *Materials Science and Engineering: A* 527 (21 – 22) 2010: pp. 5723 – 5727. https://doi.org/10.1016/j.msea.2010.05.061
44. **Davis, J.R.** Copper and copper alloys. ASM International, Materials Park, OH, USA, 2001.
45. **Ren, C., Wang, Q., Hou, J., Zhang, Z., Zhang, Z.** Effect of Work-Hardening Capacity on the Gradient Layer Properties of Metallic Materials Processed by Surface Spinning Strengthening *Materials Characterization* 177 2021: p. 111179. https://doi.org/10.1016/j.matchar.2021.111179
46. **Mubiayi, M.P., Akinlabi, E.T.** Friction Stir Spot Welding between Copper and Aluminium: Microstructural Evolution *Proceedings of the International MultiConference of Engineers and Computer Scientists (IMECS 2015)* 2 2015: pp. 1 – 5.
47. **Kah, P., Vimalraj, C., Martikainen, J., Suoranta, R.** Factors Influencing Al-Cu Weld Properties by Intermetallic

Compound Formation *International Journal of Mechanical and Materials Engineering* 10 2015: p. 10. https://doi.org/10.1186/s40712-015-0037-8

48. **Alkhafaji, A., Camas, D., Lopez-Crespo, P., Al-Asadi, H.** The Influence of Tool Geometry on the Mechanical Properties and the Microstructure of AA6061-T6 Aluminum Alloy Friction Stir Spot Welding *Materials* 16 (11) 2023: p. 4135. https://doi.org/10.3390/ma16114135
49. **Maamoun, A.H., Elbestawi, M.A., Veldhuis, S.C.** Influence of Shot Peening on AlSi10Mg Parts Fabricated by Additive Manufacturing *Journal of Manufacturing and Materials Processing* 2 (3) 2018: p. 40. https://doi.org/10.3390/jmmp2030040
50. **Qu, S., Sha, Y., Hou, Y., Wang, J., Li, F., Li, X.** Effect of Laser Shock Peening on High-Cycle Fatigue Performance and Residual Stress in DH36 Welded Joints *Materials* 18 (22) 2025: p. 5178.
51. **Nie, L., Wu, Y., Gong, H., Chen, D., Guo, X.** Effect of Shot Peening on Redistribution of Residual Stress Field in Friction Stir Welding of 2219 Aluminum Alloy *Materials* 13 (14) 2020: p. 3169. https://doi.org/10.3390/ma13143169
52. **Wang, Q., Ge, Y., Chen, J., Suzuki, T., Sagisaka, Y., Ma, N.** Unravelling Residual Stress Distribution Characteristics of 6061-T6 Aluminum Alloy Induced by Laser Shock Peening *Materials* 17 (14) 2024: p. 3484. https://doi.org/10.3390/ma17143484
53. **Cao, X., Wu, J., Zhong, G., Wu, J., Chen, X.** Laser Shock Peening: Fundamentals and Mechanisms of Metallic Material Wear Resistance Improvement *Materials* 17 (4) 2024: p. 909. https://doi.org/10.3390/ma17040909
54. **Keshavamurthy, R., Muneer, S.A.R., Nirmala Devi, E., Naga Sai, A., Ram Prasad, C., Satyanarayana, M., Venkata Ramana, V.** Influence of Shot Peening on Microstructure and Electrochemical Behavior of Al-Cu Alloy *Canadian Metallurgical Quarterly* 65 (2) 2026: pp. 1439 – 1450. https://doi.org/10.1080/00084433.2025.2518817
55. **Saai, A., Delhaye, V., Lange, T., Furu, T., Aamot, K., Lein, J.** Comparative Study of the Effects of Galvanic Corrosion on the Strength and the Failure of Aluminium and Stainless-Steel Bolted Joints *Journal of Advanced Joining Processes* 8 2023: p. 100163. https://doi.org/10.1016/j.jajp.2023.100163